



Integrated local binary pattern texture features for classification of breast tissue imaged by optical coherence microscopy



Sunhua Wan^a, Hsiang-Chieh Lee^b, Xiaolei Huang^{a,*}, Ting Xu^a, Tao Xu^c, Xianxu Zeng^{c,d}, Zhan Zhang^d, Yuri Sheikine^e, James L. Connolly^e, James G. Fujimoto^b, Chao Zhou^{c,f,g,*}

^a Department of Computer Science and Engineering, Lehigh University, Bethlehem, PA 18015, USA

^b Department of Electrical Engineering and Computer Science and Research Laboratory of Electronics, MIT, Cambridge, MA 02139, USA

^c Department of Electrical and Computer Engineering, Lehigh University, Bethlehem, PA 18015, USA

^d The Third Affiliated Hospital of Zhengzhou University, Henan, China

^e Department of Pathology, Beth Israel Deaconess Medical Center, Harvard Medical School, Boston, MA 02115, USA

^f Center for Photonics and Nanoelectronics, Lehigh University, Bethlehem, PA 18015, USA

^g Bioengineering Program, Lehigh University, Bethlehem, PA 18015, USA

ARTICLE INFO

Article history:

Received 29 July 2016

Revised 6 March 2017

Accepted 7 March 2017

Available online 8 March 2017

Keywords:

Optical coherence microscopy

Tissue classification

Texture features

Local binary patterns

ABSTRACT

This paper proposes a texture analysis technique that can effectively classify different types of human breast tissue imaged by Optical Coherence Microscopy (OCM). OCM is an emerging imaging modality for rapid tissue screening and has the potential to provide high resolution microscopic images that approach those of histology. OCM images, acquired without tissue staining, however, pose unique challenges to image analysis and pattern classification. We examined multiple types of texture features and found Local Binary Pattern (LBP) features to perform better in classifying tissues imaged by OCM. In order to improve classification accuracy, we propose novel variants of LBP features, namely average LBP (ALBP) and block based LBP (BLBP). Compared with the classic LBP feature, ALBP and BLBP features provide an enhanced encoding of the texture structure in a local neighborhood by looking at intensity differences among neighboring pixels and among certain blocks of pixels in the neighborhood. Forty-six freshly excised human breast tissue samples, including 27 benign (e.g. fibroadenoma, fibrocystic disease and usual ductal hyperplasia) and 19 breast carcinoma (e.g. invasive ductal carcinoma, ductal carcinoma in situ and lobular carcinoma in situ) were imaged with large field OCM with an imaging area of $10 \times 10 \text{ mm}^2$ ($10,000 \times 10,000$ pixels) for each sample. Corresponding H&E histology was obtained for each sample and used to provide ground truth diagnosis. 4310 small OCM image blocks (500×500 pixels) each paired with corresponding H&E histology was extracted from large-field OCM images and labeled with one of the five different classes: adipose tissue ($n = 347$), fibrous stroma ($n = 2,065$), breast lobules ($n = 199$), carcinomas (pooled from all sub-types, $n = 1,127$), and background (regions outside of the specimens, $n = 572$). Our experiments show that by integrating a selected set of LBP and the two new variant (ALBP and BLBP) features at multiple scales, the classification accuracy increased from 81.7% (using LBP features alone) to 93.8% using a neural network classifier. The integrated feature was also used to classify large-field OCM images for tumor detection. A receiver operating characteristic (ROC) curve was obtained with an area under the curve value of 0.959. A sensitivity level of 100% and specificity level of 85.2% was achieved to differentiate benign from malignant samples. Several other experiments also demonstrate the complementary nature of LBP and the two variants (ALBP and BLBP features) and the significance of integrating these texture features for classification. Using features from multiple scales and performing feature selection are also effective mechanisms to improve accuracy while maintaining computational efficiency.

© 2017 Elsevier B.V. All rights reserved.

1. Introduction

Breast cancer is a high-incidence cancer in women worldwide. It accounted for an estimated 40,000 deaths and 232,670 new cases in the United States in 2014 (American Cancer Society, 2014; Siegel et al., 2014). The survival rate of breast cancer improves with

* Corresponding authors.

E-mail addresses: xih206@lehigh.edu (X. Huang), chaozhou@lehigh.edu (C. Zhou).

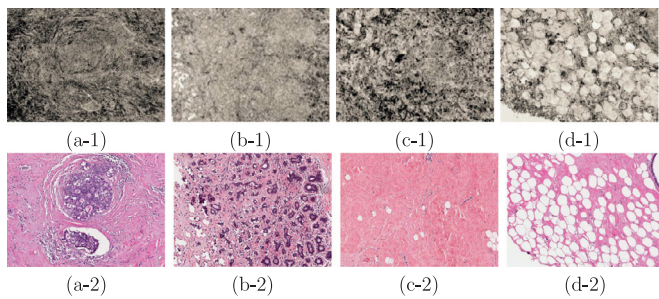


Fig. 1. Sample OCM images (first row) and corresponding histology images (second row) of human breast tissue. The ground truth labels for the tissue type of these images are: (a) carcinoma, (b) lobule, (c) stroma, (d) adipose.

screening and early detection (Boyle et al., 2008). Biopsy is a frequently used medical test in which tissue samples are removed from a human subject and then examined by a pathologist under a microscope to determine the presence or extent of a disease. Traditionally, the tissue is processed to extremely thin slices and stained before being observed under a microscope. Optical coherence tomography (OCT) provides an alternative non-invasive optical imaging modality that can provide 3D, high-resolution images of biological tissue architectures without staining (Huang et al., 1991; Fujimoto, 2003; Fujimoto et al., 2000; Tearney et al., 1997b). Optical coherence microscopy (OCM) combines the advantages of OCT and confocal microscopy using high numerical aperture objectives to provide cellular resolution images (Izatt et al., 1994; Aguirre et al., 2010b; 2010a; Ahsen et al., 2013; Lee et al., 2013).

There has been extensive research on using OCT/OCM images for analysis of human pathological samples, including skin (Gambichler et al., 2005; 2011), thyroid (Zhou et al., 2010b), breast (Zhou et al., 2010a; Assayag et al., 2014), brain (Assayag et al., 2013), gastrointestinal (Aguirre et al., 2010a; Chen et al., 2007a) and urological tissues (Tearney et al., 1997a; Zagaynova et al., 2002; Lee et al., 2012; Chen et al., 2007b). OCT images of *in vitro* atherosclerotic plaques were proved to have high resolution for intracoronary diagnostics (Brezinski et al., 1996). *In vivo* imaging of human skin using OCT is used for skin examination (Gladkova et al., 2000). OCT also enables high resolution visualization of intraretinal morphological features for macular pathology (Drexler et al., 2003; Ko et al., 2005). High resolution imaging of transitional cell carcinoma with OCT also shows feasibility for the evaluation of bladder pathology (Jesser et al., 1999). Classifying tissue types in OCT/OCM images can also be used to help diagnose breast cancer (Zhou et al., 2010a; Nguyen et al., 2009), and assist with image-guided surgery (Boppert et al., 2004; Nguyen et al., 2009; Zysk et al., 2015; Erickson-Bhatt et al., 2015). A recent study comparing OCT imaging and H&E histology of *ex vivo* breast specimens demonstrated a sensitivity of 91.7% and a specificity of 92.1% (Erickson-Bhatt et al., 2015).

Computer aided diagnosis methods based on OCT images have been proposed in previous works (Zysk and Boppert, 2006; Qi et al., 2006). Zysk et al. demonstrated the classification of tumor, stroma and adipose tissues in human breast OCT images based on spatial and frequency domain analysis (Zysk and Boppert, 2006). Qi et al. used a center-symmetric auto-correlation texture analysis method to distinguish different types of esophagus tissues in endoscopic OCT images (Qi et al., 2006). Another work (Gossage et al., 2003) proposed an automatic tissue classification method based on analyzing spectral textures in OCT images. In all these works, texture analysis is central to tissue classification, due to the characteristics of OCT/OCM images (see Fig. 1, first row).

Texture analysis has also played a central role in tissue classification for other types of medical images (Ross et al., 2006; Yao

et al., 2015; Wang et al., 2014; Toews et al., 2015). The methods used typically fall into one of two categories—structure based methods and statistical methods. Examples of structure based methods include filtering (Randen and Husoy, 1999; Jain and Farrokhnia, 1990; Chang and Kuo, 1993; Unser, 1995), textons (Varma and Zisserman, 2003), scale-invariant features such as SIFT (Toews et al., 2015), and models (Kashyap and Khotanzad, 1986; Haley and Manjunath, 1999). Examples of statistical methods include spectrum analysis (Wang and He, 1990) and feature distributions (Pietikäinen et al., 2000; Wang et al., 2014; Yao et al., 2015).

In structure based methods, typical texture patterns of an image are extracted and the frequencies of occurrence for different groups of patterns are used to represent the image. Different methods can be used to extract texture patterns. In filtering, the texture feature vectors are generated based on the local energy of filter responses. Varma et al. proposed a texton based method, which performs texture classification based on the joint distribution of intensity values over neighborhood blocks of the image (Varma and Zisserman, 2003). Toews et al. (2015) proposed a framework in which distinctive scale-invariant features such as SIFT (Lowe, 2004) are indexed in an efficient way so that approximate nearest-neighbor (NN) feature matches can be identified in $O(\log N)$ time; the NN features can then be used to assist with classification. Kashyap and Khotanzad proposed a rotation-invariant model based method (Kashyap and Khotanzad, 1986); they used a circular symmetric autoregressive model, a roughness model and a directionality model to describe textures.

In statistical methods, certain types of texture features are extracted from images and the statistical distributions of feature values are calculated and used as feature vectors for texture representation. Different texture features are used in statistical methods, including gray-level co-occurrence matrix (Marceau et al., 1990), center-symmetric auto-correlation (Harwood et al., 1995), morphological features (Wang et al., 2014), geometrical and topological features (Yao et al., 2015), gray level difference (Ojala et al., 2001), local binary patterns (LBP) (Ojala et al., 2002). Compared with structure-based methods, statistical methods are more flexible since they do not require images to contain repetitive texture patterns, and they are more suitable for analysis of OCT/OCM images of tissue samples.

In this work, we propose a breast tissue classification and abnormality detection technique based on texture analysis of *ex vivo* breast specimen imaged using an OCM system. We are particularly interested in a statistical method consisting of both training and testing steps, utilizing the LBP (Ojala et al., 2002) texture features extracted from images. In LBP, the frequencies of different local image intensity patterns are calculated and used as feature vectors (Pietikäinen et al., 2000). LBP features are rotation invariant and they have been applied in many applications, such as texture analysis (Mäenpää, 2003; Mäenpää and Pietikäinen, 2005; Ojala et al., 2000; Liao et al., 2009), face recognition (Ahonen et al., 2006; 2004; Zhang et al., 2005a; Zhao and Pietikainen, 2007; Shan et al., 2009), and description of regions of interest (Heikkilä et al., 2009). On different texture image datasets, LBP features have been used to achieve high classification accuracy (Ojala et al., 2002). In our experiments, we have found that LBP is effective in representing and classifying textures in OCT/OCM images of human breast tissue.

We introduce two new variants of LBP, average LBP (ALBP) and block based LBP (BLBP), in order to enrich texture encoding and improve classification accuracy. In the original LBP, grayscale values of a certain number of neighbor pixels are compared with the grayscale value of a center pixel to generate a binary code pattern for a local image patch. The new ALBP feature compares the grayscale value of a neighbor pixel with the average grayscale value of all neighbors; in this way, ALBP can represent the intensity differences among neighbor pixels. The new BLBP feature compares

the average intensity values of pixels in blocks of certain shape around the center pixel, thus can represent more global intensity difference information that is not captured by the original LBP features. We found that by integrating LBP features with the newly introduced two variants (ALBP and BLBP features), tissue classification accuracy can be significantly improved.

2. Image acquisition and preparation

2.1. High speed OCM system

In this study, a high speed time-domain OCM system was used to image freshly excised human breast tissue based on time domain detection techniques. The details of the system can be found in Zhou et al. (2010a); Lee et al. (2012). Briefly, a femtosecond Nd:Glass laser was spectrally broadened to generate an output spectrum centered at 1060 nm with a broad spectrum bandwidth of 200 nm, providing an axial resolution of less than 4 μ m. A 40x water immersion IR-Achroplan objective (Carl Zeiss) was used to provide OCM images with a transverse resolution of 2 μ m. Individual OCM images each covering an imaging area of 400 μ m \times 400 μ m (400 pixels \times 400 pixels, X \times Y) were acquired at a frame rate of 2 frames per sec. A high precision three-dimensional translational stage (Newport Inc.) was used allowing rapid adjustment of focus position inside the tissue and also the imaging area over the tissue surface. The entire surface of the breast tissue specimen was imaged by translating the specimen horizontally.

2.2. Specimen preparation and imaging protocol

The study protocol was approved by the institutional review boards at Beth Israel Deaconess Medical Center (BIDMC) and Massachusetts Institute of Technology (MIT). Discarded human tissue not used for routine pathologic examination was collected for the study. Freshly excised human breast tissue samples were selected based on gross pathological findings. Uninvolved, grossly normal breast tissue was also sampled. Twenty seven specimens with benign diagnosis include fibroadenoma (n = 1), benign fibrocystic disease (n = 20), and usual ductal hyperplasia (UDH, n = 6). Nineteen specimens were diagnosed as breast carcinoma including invasive ductal carcinoma (n = 16), ductal carcinoma in situ (DCIS, n = 3) and lobular carcinoma in situ (LCIS, n = 2). Note that two specimens contain both invasive ductal carcinoma and DCIS regions. Specimens (typically 1.0 cm \times 1.0 cm \times 0.5 cm) were preserved in RPMI 1640 medium (Invitrogen) prior to the imaging session and were typically imaged within 2 to 6 h after surgical resection. A thin cover glass was gently placed over a specimen's surface to create a flat imaging plane. After the imaging session, the specimen was fixed in 10% neutral buffered formalin before standard histology processing. Specimens were sectioned along the *en face* plane and stained with hematoxylin and eosin (H&E). The histopathologic diagnosis of individual breast specimens was performed by an experienced staff pathologist. Digital pathology images (Aperio, Leica Biosystem) of individual breast specimens were acquired to allow correlation between the pathologic findings and the corresponding *en face* OCM images.

2.3. Image preprocessing

The images utilized in our experiments in this work are *en face* OCM images of *ex vivo* human breast tissue. These images are contrast adjusted and displayed with an inverse grayscale color map. That means darker in OCM images represents increased reflectivity. These OCM images have an axial resolution of 4 μ m and a transverse resolution of 2 μ m respectively.

The OCM images are preprocessed for the purpose of training and testing. Fig. 2 shows an overview diagram for the training and testing processes. In the training process, each large-field OCM image, which covers an image area of about 10 \times 10 mm² (10,000 \times 10,000 pixels), is divided into small blocks (500 \times 500 pixels in our experiment). Each such small block is paired with corresponding H&E histology and labeled with one of the five different classes: adipose tissue (n = 347), fibrous stroma (n = 2,065), breast lobules (n = 199), carcinomas (pooled from all sub-types, n = 1,127), and background (regions outside of the specimens, n = 572). These image blocks with class labels are used as examples for training. Blocks of different classes show distinctive texture patterns which can serve as features for training tissue classifiers.

The ground truth labels for OCM image blocks are collected based on histology images of the same tissue specimen. Registration is performed to align and map correspondences between an OCM image and its corresponding histology image. Therefore, the histopathology result for each small block in the OCM image is known based on the class label for the corresponding block in the histology image. The class labels for each small image block in the histology image are assigned manually by an experienced pathologist. Fig. 1 shows sample OCM image blocks and their corresponding histology image blocks of human breast tissue.

For the purpose of testing, large field OCM images are divided into blocks of two different sizes. In a 10-fold cross-validation experiment, each large field OCM image is divided into blocks of 500 \times 500 pixels. These blocks are separated into ten folds where nine folds are used for training and one fold for testing. In another experiment, in order to test the robustness of our method in classifying image blocks of different sizes, the large field OCM images are divided into blocks of 400 \times 400 pixels. So image blocks of 500 \times 500 pixels are used to train the classifier, which is then tested on image blocks of 400 \times 400 pixels. By using different sized image blocks, we avoid generating the same blocks for training and testing, thus increase the reliability of our validation experiments.

3. Methodology

3.1. Feature extraction

3.1.1. Local binary patterns

Features extracted from OCM images are utilized for automatic identification of different tissue types. In this work, LBP (Ojala et al., 1996; 2002) are used as features to describe textures in a grayscale OCM image. The LBP algorithm divides the image into cells. In each cell, the intensity of a center pixel is compared to the intensity values of its neighboring pixels. The LBP feature for a local neighborhood of radius R , with P number of neighbor pixels is defined as: (Ojala et al., 2002):

$$LBP_{P,R} = \sum_{p=0}^{P-1} s(g_p - g_c) 2^p, \quad (1)$$

$$s(x) = \begin{cases} 1, & x \geq 0 \\ 0, & x < 0 \end{cases}$$

where g_c is the grayscale value of the center pixel, g_p is the gray scale value of a neighbor pixel. Fig. 3(a) shows an illustration of $LBP_{8,4}$ in which 8 neighbor pixels are located on a circle of radius 4 around the center pixel. Suppose the center pixel is located at (0,0), then the p th neighbor pixel g_p is located at $(R \sin(p \frac{2\pi}{P}), R \cos(p \frac{2\pi}{P}))$. Fig. 3(b) shows an example of obtaining a LBP feature from a local neighborhood (or cell) of an OCM image. The figure shows that the LBP feature is a pattern represented by the binary number "11100010". For $LBP_{P,R}$, there are 2^P possible binary-number patterns. To achieve rotation invariance, a function

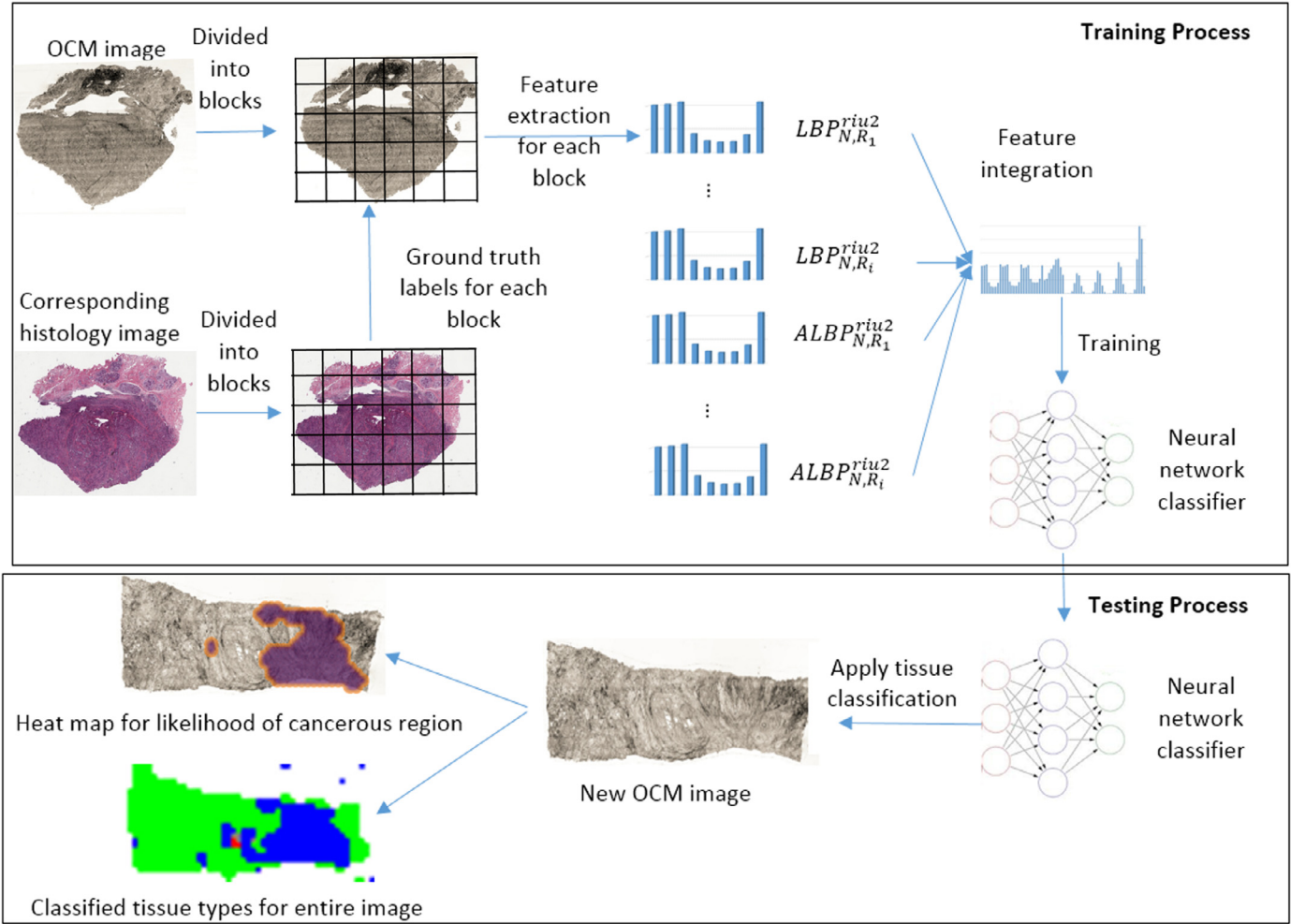


Fig. 2. Overview diagram for the training and testing processes.

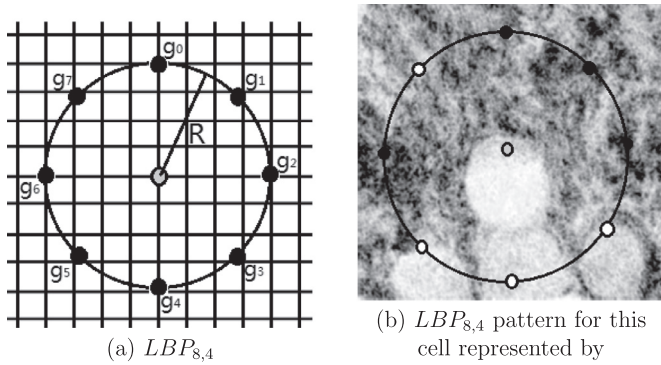


Fig. 3. Demonstration of LBP feature in a local neighborhood of an OCM image.

$U(LBP_{P,R})$ is defined as the number of 0/1 changes in a circular binary pattern:

$$U(LBP_{P,R}) = |s(g_{P-1} - g_c) - s(g_0 - g_c)| + \sum_{p=1}^{P-1} |s(g_p - g_c) - s(g_{p-1} - g_c)| \quad (2)$$

So, the LBP feature shown in Fig. 3(b) has U value of U ("11100010") = 4.

Among all the LBP patterns, the most frequent patterns are the ones with limited discontinuity in the circular binary representation thus have small U values. These patterns with small U values are also called uniform patterns because they represent local neighborhoods with relatively uniform appearance. Based on the U values, a uniform rotation-invariant feature $LBP_{P,R}^{riu2}$ is defined as:

$$LBP_{P,R}^{riu2} = \begin{cases} \sum_{p=0}^{P-1} s(g_p - g_c), & \text{if } U(LBP_{P,R}) \leq 2 \\ P + 1, & \text{otherwise} \end{cases} \quad (3)$$

Here the threshold on the U value is 2, and with this threshold, there are a total of $P + 2$ possible values for $LBP_{P,R}^{riu2}$. In our experiments, we have tried different thresholds for U value when generating features, which led to similar results. Thus we choose 2 as the threshold since $LBP_{P,R}^{riu2}$ has the smallest number of possible values and gives the shortest feature length.

To extract the rotation-invariant LBP feature vector for an $N \times N$ image, the $LBP_{P,R}^{riu2}$ value is calculated with each pixel in the image as the center pixel. Excluding those pixels that have a distance less than R from the image boundary, we get a total of $(N - 2R)^2$ $LBP_{P,R}^{riu2}$ values. The number of occurrences of each $LBP_{P,R}^{riu2}$ value in an image is calculated and represented in a histogram. The histogram is then normalized and saved as the LBP feature vector for the image, as shown in Fig. 5(c) Columns 1–9. By changing the parameters - the radius R and the number of neighbors P - a variety of LBP feature vectors can be generated for the image.

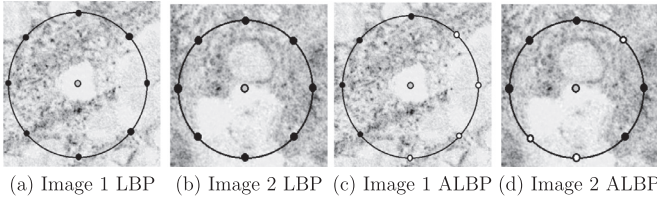


Fig. 4. Two OCM images with the same LBP feature but different ALBP features. (a),(c) are image 1; (b),(d) are image 2; (a),(b) show LBP features; (c),(d) show ALBP features.

3.1.2. Proposed novel variants of local binary patterns

In the literature, variants of LBP have been proposed to improve its performance in certain applications. Guo et al. (2010) proposed a completed LBP model which takes into consideration the magnitude of intensity difference between the center pixel and its neighbors. In this completed LBP model, the local intensity difference is divided into two complementary components: the sign and the magnitude. Experimental results in their work show that the sign component is more important than the magnitude component in representing the local features, which explains why simple LBP features have good performance. By using the integrated feature which combines the sign and magnitude components, better texture classification accuracy was reported. Tan and Triggs (2007) proposed an enhanced LBP feature which uses three states to describe the similarity of intensity values for the purpose of face recognition. In their work, local ternary patterns (LTP), a generalization of the LBP, is proposed. In LTP, the difference in local image intensity is represented as three different states. This results in a series of ternary numbers that represent local image features. LTP is tested for face recognition under different lighting conditions. Experimental results in their work show that LTP is more discriminant and more robust to noise than the original LBP feature. ul Hussain and Triggs (2012) proposed Local Quantized Patterns (LQP), which is a generalization of LBP and LTP that uses lookup-table based vector quantization instead of hand-specified codings, in order to code larger or deeper patterns. The LQP features were shown to perform very well on object detection and texture classification problems because of its run-time efficiency. Zhang et al. (2007) extended the local binary pattern operator to represent rectangular regions' intensities and the resulting binary patterns are used to describe diverse local structures of images for the purpose of face detection. Wang et al. (2009) proposed to use an integrated Histogram of Oriented Gradients (HOG) and LBP features to handle partial occlusion in human detections. By constructing an integrated detector with HOG and LBP features, their experiments show better detection performance than the original LBP features on the INRIA pedestrian dataset. Zhang et al. (2005b) proposed to integrate multi-scale and multi-orientation Gabor filters with LBP features for face representation. In their work, multi-scale and multi-orientation Gabor filters are applied on the original image to generate a set of Gabor Magnitude Pictures (GMP). Local binary patterns are then extracted based on GMPs instead of original images. The combination of Gabor filtering with LBP increased the robustness of the feature to illumination changes and noise. Zhang et al. (2010) proposed to use local derivative patterns (LDP) which use the local derivative direction variation instead of local intensity variation as the feature. In LBP, the first order local derivatives are used in describing local intensity variations; while in LDP, higher order local derivatives are used to capture more details of the local image patterns. The “nonuniform” local binary pattern is used in Zhou et al. (2008) to improve the performance in texture analysis. The original rotation-invariant LBP feature uses “uniform” patterns hence loses some information about non-uniform local neighborhoods. The work (Zhou et al., 2008)

also analyzes the structures of “nonuniform” local binary patterns and combines them with “uniform” patterns to improve texture representation. Most recently, Liu et al. (2016) developed a robust LBP variant called the Median Robust Extended Local Binary Pattern (MRELBP). In order to make LBP less sensitive to image noise, the authors proposed MRELBP that compares regional image medians rather than raw image intensities, and adopted a multiscale strategy with a novel sampling scheme to capture both microstructure and macrostructure texture information.

3.1.3. Average local binary patterns

In this work, we propose a new variant of LBP feature, namely the average LBP (ALBP) feature. Instead of comparing the intensity of a center pixel with those of its neighbors like in LBP, ALBP compares the intensity value of each neighbor pixel with the average intensity value of all neighbors:

$$ALBP_{P,R} = \sum_{p=0}^{P-1} s(g_p - g_e) 2^p, \text{ where} \quad (4)$$

$$g_e = \left(\sum_{p=0}^{P-1} g_p \right) / P$$

Note that g_e is the average intensity value of all P neighbor pixels located on a circle in a local neighborhood.

We calculate the rotation-invariant ALBP features $ALBP_{P,R}^{riu2}$ by applying the same operations that are used to transform $LBP_{P,R}^P$ to $LBP_{P,R}^{riu2}$:

$$ALBP_{P,R}^{riu2} = \begin{cases} \sum_{p=0}^{P-1} s(g_p - g_e), & \text{if } U(ALBP_{P,R}) \leq 2 \\ P + 1, & \text{otherwise} \end{cases} \quad (5)$$

By varying the parameters P and R , a variety of ALBP feature vectors can be generated for an image.

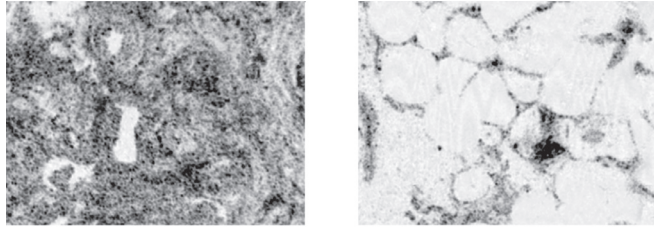
ALBP features are complementary to LBP features in describing local texture structure. A LBP feature can reveal the relationship between the center pixel and its neighbors, whereas an ALBP feature reveals more specific relations and intensity variation among the neighbors. Fig. 4 shows two different OCM image blocks that have the same LBP feature but different ALBP features in a neighborhood. Fig. 4 (a) and (b) show that the two different images both have the same LBP pattern that is represented by the binary number “11111111”; Fig. 4 (c) and (d) show that the two images have different ALBP features, which are represented by the binary numbers “10000111” and “10110011”, respectively.

Because of their complementary nature, LBP and ALBP features can be integrated to provide a richer texture feature. Fig. 5 (c) shows the integrated feature of $LBP_{8,10}^{riu2}$ and $ALBP_{8,10}^{riu2}$ for two different OCM images shown in Fig. 5 (a) and (b), respectively. In the integrated feature vector (Fig. 5(c)), Columns 1–9 represent $LBP_{8,10}^{riu2}$ and columns 10–18 represent $ALBP_{8,10}^{riu2}$. From the figure one can see that the two OCM images have similar LBP features, but significantly different ALBP features.

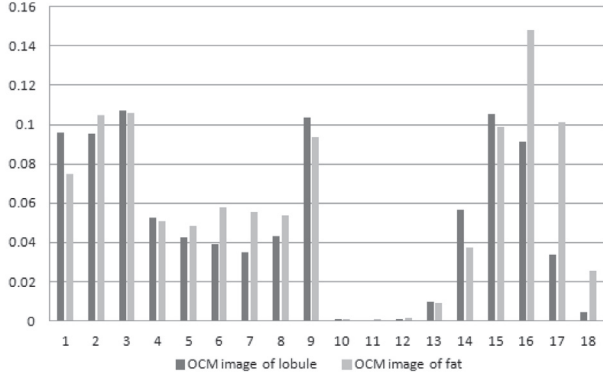
3.1.4. Block-based LBP: Spoke-LBP and Ring-LBP

In addition to ALBP, to further increase the discriminatory power of LBP texture features, we propose yet another new variant of LBP, namely the block based LBP (BLBP) features. BLBP compares the average intensity value of pixels in blocks of a certain shape in a neighborhood around the center pixel. Two different shapes of pixel blocks, namely *Spoke* and *Ring*, are used in our work, as shown in Fig. 6 (a) and (b).

The Spoke-shaped BLBP compares the intensity of the center pixel with the average intensities of neighbor pixels along P

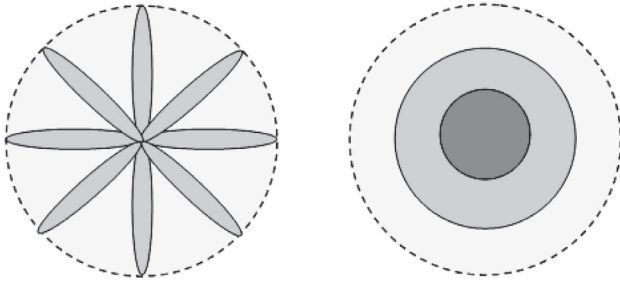
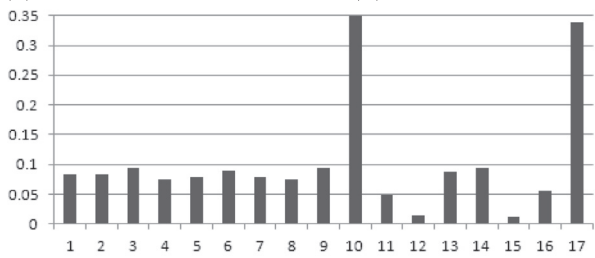


(a) OCM image of lobule tissue (b) OCM image of fat tissue



(c) Integrated LBP and ALBP feature.

Fig. 5. Integrated LBP and ALBP feature vectors for OCM images of two types of tissue. In (c), columns 1–9 represent LBP feature and columns 10–18 represent ALBP feature.

(a) Spoke-shaped *BLBP* (b) Ring-shaped *BLBP*

(c) Full *BLBP* feature for the OCM image in Figure 3 (b). Columns 1–9: $SBLBP_{8,3}$; Columns 10–17: $RBLBP_{8,1,3}$

Fig. 6. Demonstrated of Block based LBP (*BLBP*) feature.

different directions, as demonstrated in Fig. 6 (a). It can be represented as:

$$SBLBP_{P,R} = \sum_{p=0}^{P-1} s(g_{p,s} - g_c) 2^p \quad (6)$$

$$g_{p,s} = \left(\sum_{r=0}^R g_{p,r} \right) / (R + 1)$$

where $g_{p,r}$ is the gray scale value of the p th neighbor pixel on the circle with radius r , $g_{p,s}$ is the average intensity value of all the

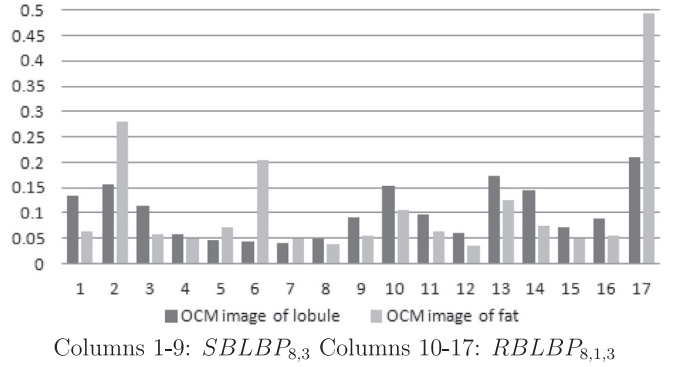


Fig. 7. *BLBP* feature vectors of the lobule and fat tissue shown in 5.

pixels along the p th neighbor's direction for all radii in $[0, R]$. We calculate the rotation-invariant features $SBLBP_{P,R}^{riu2}$ by applying the following transformation:

$$SBLBP_{P,R}^{riu2} = \begin{cases} \sum_{p=0}^{P-1} s(g_{p,s} - g_c), & \text{if } U(SBLBP_{P,R}) \leq 2 \\ P + 1, & \text{otherwise} \end{cases} \quad (7)$$

There are a total of $P + 2$ different binary-number patterns for $SBLBP_{P,R}^{riu2}$.

The Ring-shaped *BLBP* compares the intensity of the center pixel with the average intensities of neighbors in ring shaped areas around the center pixel, as demonstrated in Fig. 6 (b). It can be represented as:

$$RBLBP_{P,R,N} = \sum_{i=0}^{N-1} s(g_i - g_c) 2^i,$$

$$g_i = \left(\sum_{p=0}^{P-1} \sum_{r=i*R}^{(i+1)*R} g_{p,r} \right) / RP$$

where i is the index of the i th ring between radius $i*R$ and radius $(i + 1)*R$ around the center pixel, R is the difference of radius between two adjacent rings, N is the number of rings around the center pixel. The number of different patterns for *RBLBP* is 2^N .

By calculating the frequency of each pattern with every pixel in the image as a center pixel, we can get *SBLBP* and *RBLBP* feature vectors which are normalized histograms of pattern occurrence. The overall *BLBP* feature vector is the concatenation of the *SBLBP* and *RBLBP* feature vectors as shown in Fig. 6 (c):

$$BLBP = \{SBLBP, RBLBP\}$$

Comparing *BLBP* with *LBP*, a *BLBP* feature encodes richer information about the intensity distribution in blocks of different shape and scale in a neighborhood, whereas a *LBP* feature reveals more about the intensity differences between the center pixel and surrounding neighbor pixels. The *BLBP* feature is also more robust to noise than the *LBP* feature. Fig. 7 shows *BLBP* feature vectors for the lobule and fat tissue OCM images shown in Fig. 5. We can see that the OCM images have similar *LBP* features (Fig. 5(c)), but significantly different *BLBP* features.

3.2. Integrated multi-scale feature

Texture patterns of different scales appear in human breast tissue OCM images. *LBP* and its new *ALBP* and *BLBP* variants with different radius parameters can be used as features to capture the characteristics of texture patterns at different scales. In our work, we construct a multi-scale feature by integrating *LBP*, *ALBP* and *BLBP* features obtained with different radius parameters. Fig. 8

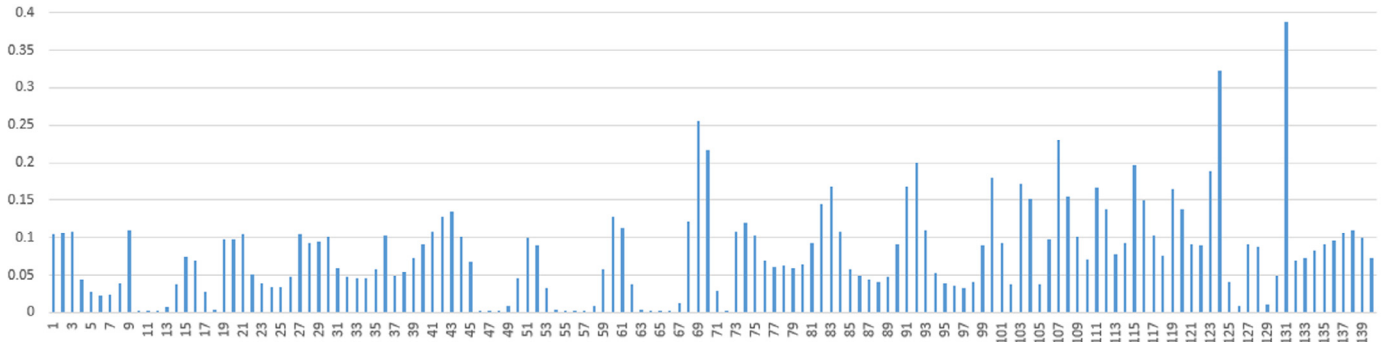


Fig. 8. Integrated multi-scale LBP+ALBP+BLBP feature vector: columns 1–9: $LBP_{8,16}^{riu2}$, columns 10–18: $LBP_{8,8}^{riu2}$, columns 19–27: $LBP_{8,4}^{riu2}$, columns 28–36: $LBP_{8,2}^{riu2}$, columns 37–45: $ALBP_{8,16}^{riu2}$, columns 46–54: $ALBP_{8,8}^{riu2}$, columns 55–63: $ALBP_{8,4}^{riu2}$, columns 64–72: $ALBP_{8,2}^{riu2}$, columns 73–81: $SBLBP_{8,3}$, columns 82–90: $SBLBP_{8,6}$, columns 91–99: $SBLBP_{8,12}$, columns 100–108: $SBLBP_{8,18}$, columns 109–116: $RBLBP_{8,13}$, columns 117–124: $RBLBP_{8,2,3}$, columns 125–132: $RBLBP_{8,4,3}$, columns 133–140: $RBLBP_{8,6,3}$.

Table 1

Classification accuracy (%) using the same texture feature ($LBP_{8,8}$) and different classifiers. The best result for each tissue class (row-wise) is highlighted in bold. Note that the neural network classifier gives the best overall performance.

Tissue type	KNN	Naive Bayes	C4.5	Neural network
Lobules	39.7	12.1	26.8	29.3
Stroma	83.6	74.2	84.0	86.2
Carcinomas	71.3	86.0	73.3	78.0
Adipose	81	55.9	78.1	80.1
Background	90.2	65.9	91.3	92.1
Total	78.9	71.8	79.1	81.7

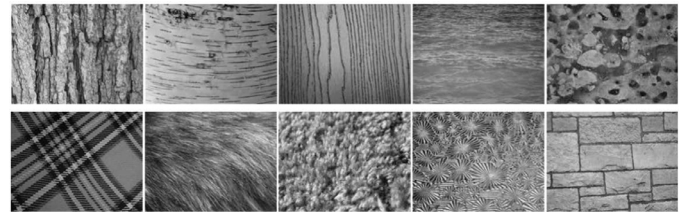


Fig. 9. Examples from UIUCTex texture image database.

shows an integrated multi-scale feature vector for an OCM image of carcinoma (tumor) tissue.

3.3. Classification algorithm

Different classification methods can be used to classify the OCM images based on LBP features. Since our focus in this paper is to introduce and integrate the new LBP features and evaluate their effects on OCM image classification, we aim to use a chosen classifier to perform many experiments employing different subsets of integrated LBP features. In order to determine which classifier to use for these tasks, we first conduct a preliminary experiment with different classifiers to classify OCM image blocks using the $LBP_{8,8}$ feature; the classifier giving the best performance in this experiment will be chosen to evaluate various subsets of integrated LBP features in Section 4.

We tested the performance of K-nearest neighbors, Naive Bayes, C4.5 decision trees, and neural network classifiers in this experiment. K-nearest neighbors (KNN) is an extensively studied classification method. It has promising performance in a variety of classification applications including image based classification (Blitzer et al., 2005). Since the features in our application are numeric features, Euclidean distance is used as the distance metric when applying the KNN classification method. Naive Bayes (NB) is a probabilistic classifier based on Bayes' theorem. C4.5 is a decision tree based classifier; it builds a predictive model that maps a feature value to an output class. Neural network (NN) classifiers are especially useful in problems that are hard to solve by rule-based classification methods, such as image classification (Giacinto and Roli, 2001). In our experiment, we used a three-layer neural network as the NN classification model. Table 1 shows the results of comparing the performance of different classification methods. From the table, one can see that the neural network classifier gives the best overall performance in this experiment. Therefore, in all our following experiments presented in Section 4, we choose to use the three-layer neural network as the classifier.

4. Experiments and results

To evaluate the performance of the proposed integrated LBP features, we conducted experiments using two sets of images: (1) texture images from commonly used datasets; and (2) human breast tissue OCM images. Experiments performed on six commonly used texture image datasets, UIUCTex, CURET, UMD, ALOT, KTHTIPS2b and Outex, are used to demonstrate the performance of the new texture features in general texture classification tasks. We compare the classification accuracy using our proposed new integrated features with that using the state-of-the-art feature, Median Robust Extended Local Binary Pattern (MRELBP) (Liu et al., 2016). The experiments performed on human breast tissue OCM images show the benefits of using the new texture features for classifying human tissue OCM images. We also compare the classification performance using the proposed integrated features with that using the LTP (Tan and Triggs, 2007), and complete local binary patterns (CLBP) (Guo et al., 2010).

4.1. Experiments on texture images

The UIUCTex texture image database includes 25 textures (Lazebnik et al., 2005). Each texture has 40 images with different scales and viewpoints. Fig. 9 shows some examples from the UIUCTex texture image database.

The CURET texture image database includes 61 textures (Dana et al., 1999). Each texture has 92 images with different viewpoints and illuminations. Fig. 10 shows some examples from the CURET texture image dataset.

The UMD high resolution image database (Xu et al., 2010) contains 25 texture classes, each with 40 images.

The ALOT database (Burghouts and Geusebroek, 2009) consists of 250 texture classes, with 100 images in each class.

The KTHTIPS2b database (Mallikarjuna et al., 2006) contains images of 11 kinds of materials, each of which has 432 images.

Classification results are evaluated by comparing the predicted class label with the ground truth class label. The evaluation process follows a 10-fold cross-validation scheme. For each dataset, all



Fig. 10. Examples from CURET texture image database.

Table 2

Classification accuracy on ALOT, KTHTIPS2b, UIUCTex, CURET and UMD datasets using different combinations of features and classifiers. *: quoted number from Liu et al. (2016); -: the result is unavailable.

Method	Integrated features		MRELBP	
	KNN	SVM	KNN	SVM
Datasets				
ALOT	0.960000	0.983160	*0.9728	-
KTHTIPS2b	0.865951	0.883838	*0.7791	*0.6913
UIUCTex	0.937	0.97	-	-
CURET	0.769331	0.883704	*0.9710	*0.9902
UMD	0.987	0.993	*0.9866	*0.9941

Table 3

Classification accuracy on OutexTC10, OutexTC12000, OutexTC12001, OutexTC36t184, OutexTC36horizon, OutexTC11[b, c, n, s] and OutexTC23[b, c, n, s] datasets using different combinations of features and classifiers. *: quoted number from Liu et al. (2016); -: the result is unavailable.

Method	Integrated features		MRELBP	
	KNN	SVM	KNN	SVM
Datasets				
OutexTC10	0.999768	0.999768	*0.9984	-
OutexTC12000	1.0	0.99875	*0.9949	-
OutexTC12001	0.999583	0.998541	*0.9977	-
OutexTC36t184	0.956897	0.934863	*0.9255	-
OutexTC36horizon	0.960449	0.931632	*0.9155	-
OutexTC11b	0.998958	1	*0.9577	-
OutexTC11c	0.996875	1	*0.9472	-
OutexTC11n	0.99375	0.996875	*0.877	-
OutexTC11s	0.983333	0.997916	*0.9984	-
OutexTC23b	0.809559	0.917647	*0.8797	-
OutexTC23c	0.803308	0.892279	*0.8036	-
OutexTC23n	0.816911	0.861397	*0.664	-
OutexTC23s	0.759926	0.792279	*0.9436	-

the images are randomly divided into 10 subsets of roughly equal size. The classification is run 10 times. In each run, a different subset is selected as test data and the remaining 9 subsets are used as training data. The final evaluation result is obtained by averaging the results over the 10 runs. The performance measurement we use is the classification accuracy:

$$\text{Accuracy} = \frac{\text{True positive} + \text{True negative}}{\text{Total number of samples}} \quad (8)$$

Tables 2 and 3 compare the average classification accuracy using the proposed integrated LBP features and the MRELBP feature (Liu et al., 2016) and with different classifiers (KNN vs SVM). For most datasets (except for CURET and OutexTC23s), the proposed integrated features can achieve similar or improved accuracy compared to MRELBP.

4.2. Classification of OCM image blocks of human breast tissue

In order to test the performance of our proposed new features on classifying tissue types in OCM images of human breast tissue, we perform classification on small OCM image blocks (500 × 500 pixels in size) obtained from the image preprocessing step (Section 2.3), using different combinations of features. Each image block is classified into one of five categories: Lobule, Stroma, Carcinoma, Adipose and Background. We used 4310 OCM image blocks

for the experiments (199 lobule, 2065 stroma, 1127 carcinoma, 347 adipose, 572 background). The classifier used was a three-layer neural network classifier (see Section 3.3). In a 10-fold 10-round cross validation, the classification accuracy values given by different feature combinations are shown in Table 4.

The feature combinations being compared in the table are:

- *MLBP*: multi-scale LBP
($LBP_{8,2}^{riu2} + LBP_{8,4}^{riu2} + LBP_{8,8}^{riu2} + LBP_{8,16}^{riu2}$)
- *MALBP*: multi-scale ALBP
($ALBP_{8,2}^{riu2} + ALBP_{8,4}^{riu2} + ALBP_{8,8}^{riu2} + ALBP_{8,16}^{riu2}$)
- *CLBP*: $CLBP_Sign + CLBP_Magnitude + CLBP_Center$
- *BLBP*: $SBLBP_{8,9} + RBLBP_{8,3,3}$
- *MBLBP*: $SBLBP_{8,3} + SBLBP_{8,6} + SBLBP_{8,12} + SBLBP_{8,18} + RBLBP_{8,1,3} + RBLBP_{8,2,3} + RBLBP_{8,4,3} + RBLBP_{8,6,3}$
- *Integrated*: $MLBP + MALBP + MBLBP$

The results shown in the column “Total” in Table 4 is the overall classification accuracy for all the image-block samples. One can see that, the multi-scale integrated feature ($MLBP + MALBP + MBLBP$) gives the best result. Since the ALBP and BLBP features are more robust to image noise and can extract richer, more distinctive information from images based on intensity variance, they demonstrated superior performance in distinguishing image blocks of different types of tissue, when integrated with original LBP. Using multi-scale features improves performance because OCM images of different tissue types exhibit different texture features at multiple scales. Our results showed that multi-scale integrated features incorporating the newly proposed ALBP and BLBP features outperformed other features in distinguishing different types of breast tissue in OCM images.

To further give a detailed depiction of the classification accuracy using the multi-scale integrated feature and three-layer neural network classifier, we show in Table 5 the confusion matrix of the classification result. One can see that very few mistakes were made on the Adipose and Background classes, whereas there were low percentages of confusion among the Lobule, Stroma and Carcinoma classes. The accuracies for all classes are above 90% except for the Lobule class (see Table 4).

4.3. Classification of large-field OCM images and tumor detection

In another experiment, we classify 46 large-field OCM images into one of two classes: all benign tissue, or tissue containing tumor. The classification of a large-field image is based on the fine-grain categorization of its subdivided blocks. In our experiment, we subdivided each large image into 400 × 400-pixel blocks. Then the fine-grain categorization process as in Section 4.2 is carried out to label each block as in one of five categories: Adipose, Stroma, Lobule, Carcinoma (pooled from all sub-types), and Background. Each category corresponds to one output value in the neural network classifier. If a large-field OCM image contains blocks that are classified as Carcinoma (i.e. cancerous tumor), the whole image is classified as tissue containing tumor; otherwise, the whole image is classified as benign.

To improve robustness of the algorithm, any isolated block (0.4mm*0.4mm in physical size) that is classified as Carcinoma is considered as noise and not taken into account during image classification. Further, since the areas in the OCM image that represent regions of cancerous tissue (i.e. Carcinoma) are determined by setting a threshold θ to the output value corresponding to Carcinoma in the neural network classifier, we can obtain a receiver operating characteristic (ROC) curve by adjusting the threshold value θ , see Fig. 11. The ROC curve can be used to characterize the performance of the large-field OCM image classification algorithm using our multi-scale integrated texture feature. The area under the

Table 4
Classification accuracy (%) using different combinations of features. The best result for each tissue class (column-wise) is highlighted in bold.

Features	Lobule	Stroma	Carcinoma	Adipose	Background	Total
<i>LBP</i> _{2,8}	7.1	81.5	73.4	30.5	58.7	68.8
<i>LBP</i> _{4,8}	23.2	82.2	75.7	69.2	77.1	76.1
<i>LBP</i> _{8,2}	53.5	86.0	72.8	46.7	88.3	78.2
<i>LBP</i> _{8,4}	39.9	86.3	77.7	79.5	87.4	81.6
<i>LBP</i> _{8,8}	29.3	86.2	78.0	80.1	92.1	81.7
<i>LBP</i> _{8,16}	25.3	81.6	60.5	69.7	87.6	73.4
<i>LBP</i> _{8,8} , <i>ALBP</i> _{8,8}	31.8	86.9	79.8	87.9	97.7	84.0
<i>MLBP</i> , <i>MALBP</i>	61.1	92.3	85.4	94.2	99.3	90.2
<i>BLBP</i>	59.3	88.2	84.6	88.8	99.1	87.4
<i>MBLBP</i>	77.4	96.2	83.2	95.9	100	92.4
<i>Integrated</i>	68.3	94.0	93.5	97.1	100	93.8
<i>LTP</i> _{8,8}	10.6	86.4	81.4	90.5	93.9	82.9
<i>CLBP</i>	57.3	89.6	73.8	81.8	99.0	84.6

Table 5
Confusion matrix of the classification result obtained by multi-scale integrated feature and neural network classifier.

		Predicted class				
		Lobule	Stroma	Carcinoma	Adipose	Background
Actual class	Lobules	136	20	40	3	0
	Stroma	2	1942	121	0	0
	Carcinoma	3	70	1054	0	0
	Adipose	3	7	0	337	0
	Background	0	0	0	0	572

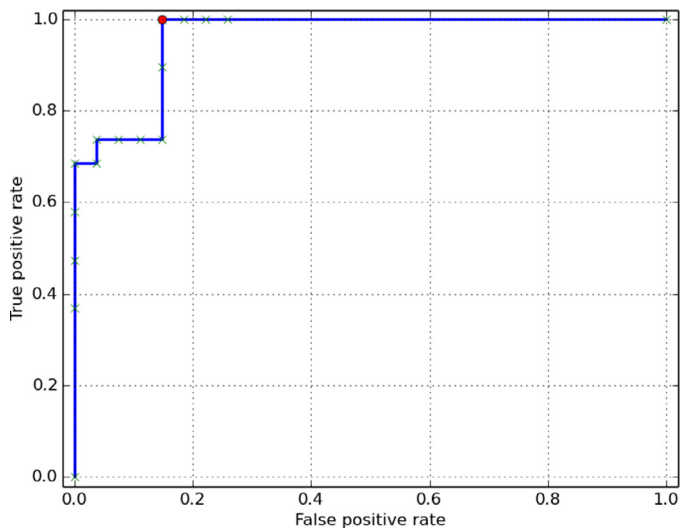


Fig. 11. ROC curve for tumor tissue detection in large-field OCM images. (For interpretation of the references to colour in the text, the reader is referred to the web version of this article.)

curve (AUC) value is found to be 0.959. The best classification accuracy is obtained at a sensitivity level of 100% and specificity level of 85.2% (marked by red circle in Fig. 11).

For comparison, the classification accuracies using different texture features are shown in Table 6. The best performance is achieved using the integrated feature, as well as MBLBP feature, on the two-class large-field OCM image classification task. The confusion matrix for the classification result using integrated feature (*MLBP* + *MALBP* + *MBLBP*) is shown in Table 7.

Fig. 12 shows some of the results of breast tissue OCM image classification using multi-scale integrated feature (*LBP* + *ALBP* + *BLBP*). The first column is the histology images that are used as the ground truth to evaluate the classification accuracy. The second column is the corresponding OCM images used as test data.

Table 6
Accuracy (%) of large-field OCM image classification using different features. MBLBP: Multi-scale BLBP; MALBP: Multi-scale ALBP (Wan et al., 2014).

		Feature Type				
		Integrated	MBLBP	MALBP	LBP	CLBP
Image	Containing Tumor	100	100	94.7	57.9	73.7
	All Benign	85.2	85.2	85.2	74.1	81.5
	Total	91.3	91.3	89.1	67.4	78.2

Table 7
Confusion matrix of large-field OCM image classification obtained by multi-scale integrated feature.

		Predicted class	
		Containing Tumor	All Benign
Actual image class	Containing Tumor	19	0
	All Benign	4	23

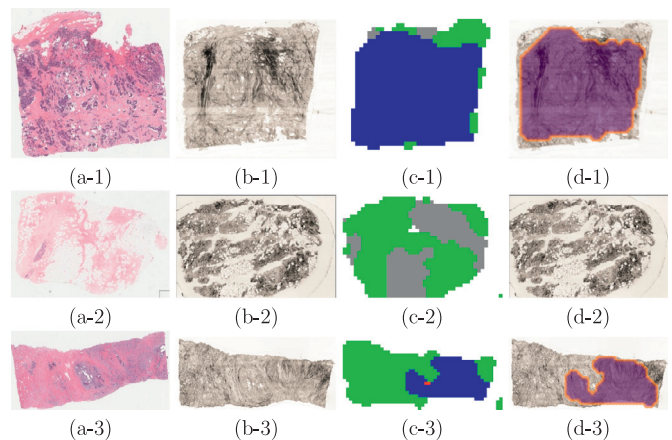


Fig. 12. Breast tissue OCM image classification results. The results include two classes of images: image of tissue with tumor (image 1 and 3), and image of tissue without tumor (image 2). (a) histology image; (b) OCM image; (c) classification result; (d) probability distribution (i.e. heat map) of tumor tissue.

third column in Fig. 12 (c) shows the color map of the classification result, with each color representing a tissue type (white: background, blue: carcinoma, red: lobules, green: stroma, grey: adipose). Based on the classification results, we also generate heat maps that indicate tumor regions as shown in the last column, Fig. 12 (d); the purple overlay indicates high-probability tumor regions.

5. Discussion

5.1. Algorithm limitation

Using integrated imaging features, our algorithm demonstrated over 90% overall accuracy in differentiating benign and malignant specimens (Table 6). Four benign specimens were falsely diagnosed as malignant based on large-field OCM images (Table 7). Two of these specimens were obtained from previous biopsy sites and one was a specimen containing usual ductal hyperplasia (UDH). A closer look of Table 5 shows that many of the mis-classified cases are misclassifying lobules as carcinomas. The algorithm's accuracy on classifying lobules is lower than classifying other categories of tissues. We speculate that the reason is because in OCM images, lobules are visually more similar to carcinomas than other types of tissues. Our texture features were not able to extract enough information from the OCM images to clearly separate normal lobules or lobules with inflammation from carcinomas. Another type of mis-classification is between carcinomas and stromas. In some tumor specimens, cancer cells are sparsely distributed within the stromas; our features give lower classification accuracy on these sparsely distributed carcinoma tissues than dense carcinoma tissues.

5.2. Attribute selection

In order to increase the speed of the classification algorithm, the integrated feature can be evaluated in an attribute selection phase, so that only the most representative attributes in the integrated feature are selected to be used to construct the classifier. During an attribute selection step, attributes that can represent distinctive characteristics of different types of tissues should be kept while less relevant attributes are eliminated, in order to lower the dimension of the feature vector and reduce computational complexity for both training and testing. Attribute selection typically consists of two components: a search method that extracts a new subset of attributes from the original attribute space, and an evaluation method that assigns a score to any attribute subset. Commonly used search methods include greedy forward selection, simulated annealing, genetic algorithm (Yang and Honavar, 1998), among others. Commonly used evaluation methods include information gain, Chi-square, among others.

In our work, we did an experiment to perform attribute selection on the attributes of the integrated multi-scale LBP+ALBP+BLBP feature vector. We used information gain as the evaluation method and attribute subsets were ranked according to their individual evaluation scores in order to achieve fast and accurate subset selection. As a result of the selection, the dimension of the feature set for training and testing was reduced from 140 to 24. Fig. 13 shows the average value for each of the 140-dimensional features of four different types of tissues and background; the average values for consecutive features of the same tissue class are connected to form one line per class. All together, the five colored lines for the five classes (i.e. lobule, stroma, carcinoma, adipose, and background) form a line graph from which one can visually see which features exhibit different values for different classes. Our attribute selection algorithm based on information gain evaluation selected

24 top features which are marked by red squares along the horizontal axis of the graph in Fig. 13. From the figure, one can see that 7 of the selected features are from LBP features, 2 selected features are from ALBP features and the rest 15 selected features are from BLBP features.

In this experiment, by attribute selection and reducing the dimension of the feature vector from 140 to 24, the running time for training a classifier was reduced by 4.8%. The classification accuracy dropped slightly though, after attribute selection; without attribute selection and using the full 140-dimensional feature vector, classification accuracy was 93.8% whereas accuracy was 87.0% using the 24-dimensional feature vector of selected attributes.

5.3. Application of ALBP and BLBP to other types of images

The proposed ALBP and BLBP methods extract texture features based on comparison of relative pixel intensity in an image, and they are not limited to any specific imaging modality, such as OCM. ALBP and BLBP could also be used for H&E stain image analysis. As a future direction, we plan to perform experiments that use ALBP and BLBP for classifying H&E images and also compare the performance of classification based on multi-modal images (e.g. OCM and H&E together) vs. that of classification using a single modality image.

5.4. Potential of deep features

Convolutional neural networks (CNN) and deep features have become very popular in recent research and are increasingly used in a wide range of applications for recognition and segmentation. Deep features have been successfully applied to texture recognition (Cimpoi et al., 2015) and to improving the performance of various computer-aided diagnosis applications such as classifying skin lesion images (Kawahara et al., 2015), lung diseases and colonic polyps (Roth et al., 2016). Cimpoi et al. (2015) proposed a new texture descriptor, FV-CNN, which is obtained by Fish Vector Pooling of a CNN filter bank, and used it to achieve state-of-the-art performance in recognizing material texture on Flickr material dataset and in scene recognition on MIT indoor scenes dataset. Kawahara et al. (2015) investigated whether filters and deep features learned in a CNN trained on natural images would generalize well to classifying skin lesion images; their conclusion was that such deep features do provide performance improvement over published results that did not use deep features. They further improved the standard CNN as a feature extractor approach by using normalization, a multi-scale scheme and pooling across an augmented feature space. Roth et al. (2016) address the training data issue for CNN in medical imaging by generating novel 2D or 2.5D image views via sampling through scale transformations, random translations and rotations. In testing, the trained CNN assigns class (e.g. lesion, pathology) probabilities for a new set of random views that are then averaged to compute a final classification probability. As these research studies have shown, CNN and deep features generalize well to different medical image classification applications and can scale to data sets of various sizes. In our future work, we plan to investigate the potential application of deep features for classifying OCT/OCM images of tissue samples. We foresee the main challenges to be collecting a sufficient amount of training data to fine tune pre-trained deep features and providing accurate semantic labels to texture patches that appear in OCT/OCM tissue images.

6. Conclusions

This paper introduces texture analysis techniques applied on OCM images to achieve automatic classification of human breast tissues. New variants of LBP features, ALBP and BLBP, are proposed.

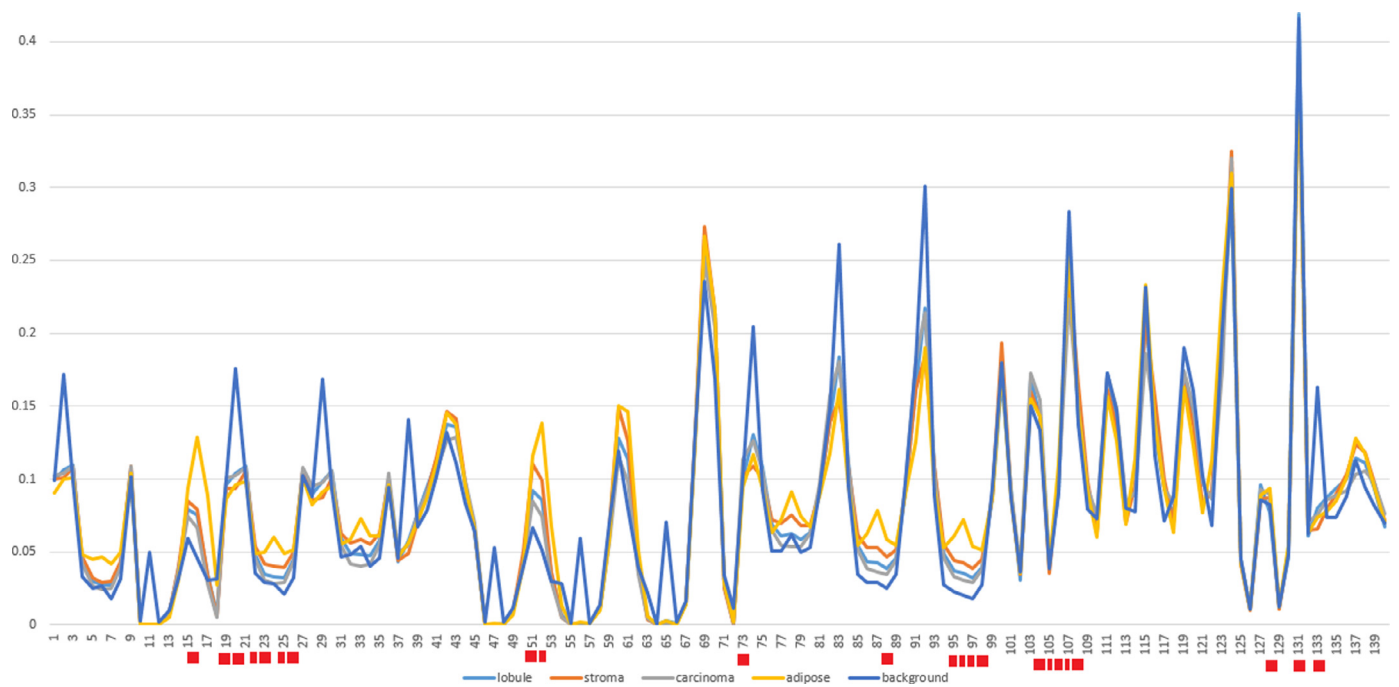


Fig. 13. Average feature values for five different classes of OCM image blocks and demonstration of attribute selection. The total dimension of a feature vector is 140. 24 attributes are selected by the information gain based attribute selection algorithm. The selected 24 are marked by red squares along the horizontal axis. Dimension 1–9: $LBP_{8,16}^{riu2}$, dimension 10–18: $LBP_{8,8}^{riu2}$, dimension 19–27: $LBP_{8,4}^{riu2}$, dimension 28–36: $LBP_{8,2}^{riu2}$, dimension 37–45: $ALBP_{8,16}^{riu2}$, dimension 46–54: $ALBP_{8,8}^{riu2}$, dimension 55–63: $ALBP_{8,4}^{riu2}$, dimension 64–72: $ALBP_{8,2}^{riu2}$, dimension 73–81: $SBLBP_{8,3}$, dimension 82–90: $SBLBP_{8,6}$, dimension 91–99: $SBLBP_{8,12}$, dimension 100–108: $SBLBP_{8,18}$, dimension 109–116: $RBLBP_{8,13}$, dimension 117–124: $RBLBP_{8,2,3}$, dimension 125–132: $RBLBP_{8,4,3}$, dimension 133–140: $RBLBP_{8,6,3}$. (For interpretation of the references to colour in this figure legend, the reader is referred to the web version of this article.)

The new variants are more robust to image noise and extract richer texture information from images than the original LBP features. Thus by integrating these new variants with the original LBP features, we were able to achieve more accurate image classification in our experiments. The promising results from our work suggest the potential of using texture analysis of OCM images to assist with diagnosis of breast cancer.

Acknowledgements

This work was supported by the NSF grant 1455613 to C. Zhou, NIH grants: R00-EB010071 and R21-EY026380 to C. Zhou, R01-GM098430 to X. Huang, and R01-CA75289-18, R01-CA178636-03 to J.G. Fujimoto and J.L. Connolly.

References

Aguirre, A.D., Chen, Y., Bryan, B., Mashimo, H., Connolly, J.L., Fujimoto, J.G., Huang, Q., 2010. Cellular resolution ex vivo imaging of gastrointestinal tissues with optical coherence microscopy. *J. Biomed. Opt.* 15 (1), 016025–016025.

Aguirre, A.D., Sawinski, J., Huang, S.-W., Zhou, C., Denk, W., Fujimoto, J.G., 2010. High speed optical coherence microscopy with autofocus adjustment and a miniaturized endoscopic imaging probe. *Opt. Express* 18 (5), 4222–4239.

Ahonen, T., Hadid, A., Pietikainen, M., 2004. Face recognition with local binary patterns. In: *Computer Vision-ECCV 2004*. Springer, pp. 469–481.

Ahonen, T., Hadid, A., Pietikainen, M., 2006. Face description with local binary patterns: application to face recognition. *Pattern Anal. Mach. Intell. IEEE Trans.* 28 (12), 2037–2041.

Ahsen, O.O., Tao, Y.K., Potsaid, B.M., Shekine, Y., Jiang, J., Grulkowski, I., Tsai, T.-H., Jayaraman, V., Kraus, M.F., Connolly, J.L., et al., 2013. Swept source optical coherence microscopy using a 1310 nm vcsel light source. *Opt. Express* 21 (15), 18021–18033.

American Cancer Society, 2014. *Cancer facts & figures 2014*.

Assayag, O., Antoine, M., Sigal-Zafrani, B., Riben, M., Harms, F., Burcheri, A., Grieve, K., Dalimier, E., Le Conte de Poly, B., Boccard, C., 2014. Large field, high resolution full-field optical coherence tomography: a pre-clinical study of human breast tissue and cancer assessment. *Technol. Cancer Res. Treat.* 13 (5), 455–468.

Assayag, O., Grieve, K., Devaux, B., Harms, F., Pallud, J., Chretien, F., Boccard, C., Varlet, P., 2013. Imaging of non-tumorous and tumorous human brain tissues with full-field optical coherence tomography. *NeuroImage: clinical* 2, 549–557.

Blitzer, J., Weinberger, K.Q., Saul, L.K., 2005. Distance metric learning for large margin nearest neighbor classification. In: *Advances in Neural Information Processing Systems*, pp. 1473–1480.

Boppart, S.A., Luo, W., Marks, D.L., Singletary, K.W., 2004. Optical coherence tomography: feasibility for basic research and image-guided surgery of breast cancer. *Breast Cancer Res. Treat.* 84 (2), 85–97.

Boyle, P., Levin, B., et al., 2008. *World Cancer Report 2008*. IARC Press, International Agency for Research on Cancer.

Brezinski, M.E., Tearney, G.J., Bouma, B.E., Izatt, J.A., Hee, M.R., Swanson, E.A., Southern, J.F., Fujimoto, J.G., 1996. Optical coherence tomography for optical biopsy properties and demonstration of vascular pathology. *Circulation* 93 (6), 1206–1213.

Burghouts, G.J., Geusebroek, J.-M., 2009. Material-specific adaptation of color invariant features. *Pattern. Recognit. Lett.* 30 (3), 306–313.

Chang, T., Kuo, C.-C., 1993. Texture analysis and classification with tree-structured wavelet transform. *Image Process. IEEE Trans.* 2 (4), 429–441.

Chen, Y., Aguirre, A., Hsiung, P.-L., Desai, S., Herz, P., Pedrosa, M., Huang, Q., Figueiredo, M., Huang, S.-W., Koski, A., et al., 2007. Ultrahigh resolution optical coherence tomography of Barretts esophagus: preliminary descriptive clinical study correlating images with histology. *Endoscopy* 39 (07), 599–605.

Chen, Y., Andrews, P.M., Aguirre, A.D., Schmitt, J.M., Fujimoto, J.G., 2007. High-resolution three-dimensional optical coherence tomography imaging of kidney microanatomy ex vivo. *J. Biomed. Opt.* 12 (3), 034008–034008.

Cimpoi, M., Maji, S., Kokkinos, I., Vedaldi, A., 2015. Deep filter banks for texture recognition, description, and segmentation. *Int. J. Comput. Vision* 118 (1), 65–94.

Dana, K.J., Van Ginneken, B., Nayar, S.K., Koenderink, J.J., 1999. Reflectance and texture of real-world surfaces. *ACM Trans. Graphics (TOG)* 18 (1), 1–34.

Drexler, W., Sattmann, H., Hermann, B., Ko, T.H., Stur, M., Unterhuber, A., Scholda, C., Findl, O., Wirtitsch, M., Fujimoto, J.G., et al., 2003. Enhanced visualization of macular pathology with the use of ultrahigh-resolution optical coherence tomography. *Arch. Ophthalmol.* 121 (5), 695–706.

Erickson-Bhatt, S.J., Nolan, R.M., Shemonski, N.D., Adie, S.G., Putney, J., Darga, D., McCormick, D.T., Cittadine, A.J., Zysk, A.M., Marjanovic, M., Chaney, E.J., Monroy, G.L., South, F.A., Craddock, K.A., Liu, Z.G., Sundaram, M., Ray, P.S., Boppart, S.A., 2015. Real-time imaging of the resection bed using a handheld probe to reduce incidence of microscopic positive margins in cancer surgery. *Cancer Res.* 75 (18), 3706–3712.

Fujimoto, J.G., 2003. Optical coherence tomography for ultrahigh resolution in vivo imaging. *Nat. Biotechnol.* 21 (11), 1361–1367.

- Fujimoto, J.G., Pitris, C., Boppart, S.A., Brezinski, M.E., 2000. Optical coherence tomography: an emerging technology for biomedical imaging and optical biopsy. *Neoplasia* 2 (1), 9–25.
- Gambichler, T., Jaedicke, V., Terras, S., 2011. Optical coherence tomography in dermatology: technical and clinical aspects. *Arch. Dermatol. Res.* 303 (7), 457–473.
- Gambichler, T., Moussa, G., Sand, M., Sand, D., Altmeyer, P., Hoffmann, K., 2005. Applications of optical coherence tomography in dermatology. *J. Dermatol. Sci.* 40 (2), 85–94.
- Giacinto, G., Roli, F., 2001. Design of effective neural network ensembles for image classification purposes. *Image Vis. Comput.* 19 (9), 699–707.
- Gladkova, N.D., Petrova, G., Nikulin, N., Radenska-Lopovok, S., Snopova, L., Chumakov, Y.P., Nasonova, V., Gelikonov, V., Gelikonov, G., Kuranov, R., et al., 2000. In vivo optical coherence tomography imaging of human skin: norm and pathology. *Skin Res. Technol.* 6 (1), 6–16.
- Gossage, K.W., Tkaczyk, T.S., Rodriguez, J.J., Barton, J.K., 2003. Texture analysis of optical coherence tomography images: feasibility for tissue classification. *J. Biomed. Opt.* 8 (3), 570–575.
- Guo, Z., Zhang, L., Zhang, D., 2010. A completed modeling of local binary pattern operator for texture classification. *Image Process. IEEE Trans.* 19 (6), 1657–1663.
- Haley, G.M., Manjunath, B., 1999. Rotation-invariant texture classification using a complete space-frequency model. *Image Process. IEEE Trans.* 8 (2), 255–269.
- Harwood, D., Ojala, T., Pietikäinen, M., Kelman, S., Davis, L., 1995. Texture classification by center-symmetric auto-correlation, using kullback discrimination of distributions. *Pattern Recognit. Lett.* 16 (1), 1–10.
- Heikkilä, M., Pietikäinen, M., Schmid, C., 2009. Description of interest regions with local binary patterns. *Pattern Recognit.* 42 (3), 425–436.
- Huang, D., Swanson, E.A., Lin, C.P., Schuman, J.S., Stinson, W.G., Chang, W., Hee, M.R., Flotte, T., Gregory, K., Puliafito, C.A., et al., 1991. Optical coherence tomography. *Science* 254 (5035), 1178–1181.
- Izatt, J., Hee, M., Owen, G., Swanson, E.A., Fujimoto, J., 1994. Optical coherence microscopy in scattering media. *Opt. Lett.* 19 (8), 590–592.
- Jain, A.K., Farrokhnia, F., 1990. Unsupervised texture segmentation using gabor filters. In: *Systems, Man and Cybernetics, 1990. Conference Proceedings., IEEE International Conference on.* IEEE, pp. 14–19.
- Jesser, C., Boppart, S., Pitris, C., Stamper, D., Nielsen, G.P., Brezinski, M., Fujimoto, J., 1999. High resolution imaging of transitional cell carcinoma with optical coherence tomography: feasibility for the evaluation of bladder pathology. *Br. J. Radiol.* 72 (864), 1170–1176.
- Kashyap, R.L., Khotanad, A., 1986. A model-based method for rotation invariant texture classification. *Pattern Anal. Mach. Intell. IEEE Trans.* 8 (4), 472–481.
- Kawahara, J., BenTaieb, A., Hamarneh, G., 2015. Deep features to classify skin lesions. Ko, T.H., Fujimoto, J.G., Schuman, J.S., Paunescu, L.A., Kowalewicz, A.M., Hartl, I., Drexler, W., Wollstein, G., Ishikawa, H., Duker, J.S., 2005. Comparison of ultra-high and standard-resolution optical coherence tomography for imaging macular pathology. *Ophthalmology* 112 (11), 1922–e1.
- Lazebnik, S., Schmid, C., Ponce, J., 2005. A sparse texture representation using local affine regions. *Pattern Anal. Mach. Intell. IEEE Trans.* 27 (8), 1265–1278.
- Lee, H.-C., Liu, J.J., Sheikine, Y., Aguirre, A.D., Connolly, J.L., Fujimoto, J.G., 2013. Ultra-high speed spectral-domain optical coherence microscopy. *Biomed. Opt. Express* 4 (8), 1236–1254.
- Lee, H.-C., Zhou, C., Cohen, D.W., Mondelblatt, A.E., Wang, Y., Aguirre, A.D., Shen, D., Sheikine, Y., Fujimoto, J.G., Connolly, J.L., 2012. Integrated optical coherence tomography and optical coherence microscopy imaging of ex vivo human renal tissues. *J. Urol.* 187 (2), 691–699.
- Liao, S., Law, M.W., Chung, A.C., 2009. Dominant local binary patterns for texture classification. *Image Process. IEEE Trans.* 18 (5), 1107–1118.
- Liu, L., Lao, S., Fieguth, P.W., Guo, Y., Wang, X., Pietikäinen, M., 2016. Median robust extended local binary pattern for texture classification. *IEEE Trans. Image Process.* 25 (3), 1368–1381.
- Lowe, D.G., 2004. Distinctive image features from scale-invariant keypoints. *Int. J. Comput. Vis.* 60 (2), 91–110.
- Mäenpää, T., 2003. The local binary pattern approach to texture analysis: Extensions and applications. *Oulun yliopisto.*
- Mäenpää, T., Pietikäinen, M., 2005. Texture analysis with local binary patterns. In: *Handbook of Pattern Recognition and Computer Vision*, 3, pp. 197–216.
- Mallikarjuna, P., Fritz, M., Targhi, A. T., Hayman, E., Caputo, B., Eklundh, J., 2006. The kth-tips and kth-tips2 databases.
- Marceau, D.J., Howarth, P.J., Dubois, J.-M.M., Gratton, D.J., et al., 1990. Evaluation of the grey-level co-occurrence matrix method for land-cover classification using spot imagery. *IEEE Trans. Geosci. Remote Sens.* 28 (4), 513–519.
- Nguyen, F.T., Zysk, A.M., Chaney, E.J., Kotynek, J.G., Oliphant, U.J., Bellafiore, F.J., Rowland, K.M., Johnson, P.A., Boppart, S.A., 2009. Intraoperative evaluation of breast tumor margins with optical coherence tomography. *Cancer Res.* 69 (22), 8790–8796.
- Ojala, T., Pietikäinen, M., Harwood, D., 1996. A comparative study of texture measures with classification based on featured distributions. *Pattern Recognit.* 29 (1), 51–59.
- Ojala, T., Pietikäinen, M., Mäenpää, T., 2000. Gray scale and rotation invariant texture classification with local binary patterns. In: *Computer Vision-ECCV 2000.* Springer, pp. 404–420.
- Ojala, T., Pietikäinen, M., Maenpaa, T., 2002. Multiresolution gray-scale and rotation invariant texture classification with local binary patterns. *Pattern Anal. Mach. Intell. IEEE Trans.* 24 (7), 971–987.
- Ojala, T., Valkealahti, K., Oja, E., Pietikäinen, M., 2001. Texture discrimination with multidimensional distributions of signed gray-level differences. *Pattern Recognit.* 34 (3), 727–739.
- Pietikäinen, M., Ojala, T., Xu, Z., 2000. Rotation-invariant texture classification using feature distributions. *Pattern Recognit.* 33 (1), 43–52.
- Qi, X., Sivak, M.V., Isenberg, G., Willis, J.E., Rollins, A.M., 2006. Computer-aided diagnosis of dysplasia in barretts esophagus using endoscopic optical coherence tomography. *J. Biomed. Opt.* 11 (4), 044010–044010.
- Randen, T., Husoy, J.H., 1999. Filtering for texture classification: a comparative study. *Pattern Anal. Mach. Intell. IEEE Trans.* 21 (4), 291–310.
- Ross, N.E., Pritchard, C.J., Rubin, D.M., Duse, A.G., 2006. Automated image processing method for the diagnosis and classification of malaria on thin blood smears. *Med. Biol. Eng. Comput.* 44 (5), 427–436.
- Roth, H.R., Lu, L., Liu, J., Yao, J., Seff, A., Cherry, K., Kim, L., Summers, R.M., 2016. Improving computer-aided detection using convolutional neural networks and random view aggregation. *Med. Imaging, IEEE Trans.* 35, 1170–1181.
- Shan, C., Gong, S., McOwan, P.W., 2009. Facial expression recognition based on local binary patterns: a comprehensive study. *Image Vision Comput.* 27 (6), 803–816.
- Siegel, R., Ma, J., Zou, Z., Jemal, A., 2014. Cancer statistics, 2014. *CA: Cancer J. Clin.* 64 (1), 9–29.
- Tan, X., Triggs, B., 2007. Enhanced local texture feature sets for face recognition under difficult lighting conditions. In: *Analysis and Modeling of Faces and Gestures.* Springer, pp. 168–182.
- Tearney, G., Brezinski, M., Southern, J., Bouma, B., Boppart, S., Fujimoto, J., 1997. Optical biopsy in human urologic tissue using optical coherence tomography. *J. Urol.* 157 (5), 1915–1919.
- Tearney, G.J., Brezinski, M.E., Bouma, B.E., Boppart, S.A., Pitris, C., Southern, J.F., Fujimoto, J.G., 1997. In vivo endoscopic optical biopsy with optical coherence tomography. *Science* 276 (5321), 2037–2039.
- Toews, M., Wachinger, C., Estepar, R., Wells, W., 2015. A feature-based approach to big data analysis of medical images, 339–350.
- ul Hussain, S., Triggs, B., 2012. Visual recognition using local quantized patterns. *Lect. Notes Comput. Sci.—ECCV Proc.* 7573, 716–729.
- Unser, M., 1995. Texture classification and segmentation using wavelet frames. *Image Process. IEEE Trans.* 4 (11), 1549–1560.
- Varma, M., Zisserman, A., 2003. Texture classification: are filter banks necessary? In: *Computer Vision and Pattern Recognition, 2003. Proceedings. 2003 IEEE Computer Society Conference on.* IEEE, pp. 11–691.
- Wan, S., Lee, H.-C., Fujimoto, J.G., Huang, X., Zhou, C., 2014. Ocm image texture analysis for tissue classification. In: *Biomedical Imaging (ISBI), 2014 IEEE 11th International Symposium on.* IEEE, pp. 93–96.
- Wang, H., Xing, F., Su, H., Stromberg, A., Yang, L., 2014. Novel image markers for non-small cell lung cancer classification and survival prediction. *BMC Bioinf.* 15, 1–12.
- Wang, L., He, D.-C., 1990. Texture classification using texture spectrum. *Pattern Recognit.* 23 (8), 905–910.
- Wang, X., Han, T.X., Yan, S., 2009. An hog-lbp human detector with partial occlusion handling. In: *Computer Vision, 2009 IEEE 12th International Conference on.* IEEE, pp. 32–39.
- Xu, Y., Yang, X., Ling, H., Ji, H., 2010. A new texture descriptor using multifractal analysis in multi-orientation wavelet pyramid. In: *Computer Vision and Pattern Recognition (CVPR), 2010 IEEE Conference on.* IEEE, pp. 161–168.
- Yang, J., Honavar, V., 1998. Feature subset selection using a genetic algorithm. In: *Feature Extraction, Construction and Selection.* Springer, pp. 117–136.
- Yao, J., Ganti, D., Luo, X., Xiao, G., Xie, Y., Yan, S., Huang, J., 2015. Computer-assisted diagnosis of lung cancer using quantitative topology features, 288–295.
- Zagaynova, E.V., Streltsova, O.S., Gladkova, N.D., Snopova, L.B., Gelikonov, G.V., Feldchtein, F.I., Morozov, A.N., 2002. In vivo optical coherence tomography feasibility for bladder disease. *J. Urol.* 167 (3), 1492–1496.
- Zhang, B., Gao, Y., Zhao, S., Liu, J., 2010. Local derivative pattern versus local binary pattern: face recognition with high-order local pattern descriptor. *Image Process. IEEE Trans.* 19 (2), 533–544.
- Zhang, G., Huang, X., Li, S.Z., Wang, Y., Wu, X., 2005. Boosting local binary pattern (lbp)-based face recognition. In: *Advances in biometric person authentication.* Springer, pp. 179–186.
- Zhang, L., Chu, R., Xiang, S., Liao, S., Li, S.Z., 2007. Face detection based on multi-block lbp representation. *Lect. Notes Comput. Sci.—Proc. Adv. Biometrics Conf.* 4642, 11–18.
- Zhang, W., Shan, S., Gao, W., Chen, X., Zhang, H., 2005. Local gabor binary pattern histogram sequence (lgbphs): a novel non-statistical model for face representation and recognition. In: *Computer Vision, 2005. ICCV 2005. Tenth IEEE International Conference on.* IEEE, pp. 786–791.
- Zhao, G., Pietikainen, M., 2007. Dynamic texture recognition using local binary patterns with an application to facial expressions. *Pattern Anal. Mach. Intell. IEEE Trans.* 29 (6), 915–928.
- Zhou, C., Cohen, D.W., Wang, Y., Lee, H.-C., Mondelblatt, A.E., Tsai, T.-H., Aguirre, A.D., Fujimoto, J.G., Connolly, J.L., 2010. Integrated optical coherence tomography and microscopy for ex vivo multiscale evaluation of human breast tissues. *Cancer Res.* 70 (24), 10071–10079.
- Zhou, C., Wang, Y., Aguirre, A.D., Tsai, T.-H., Cohen, D.W., Fujimoto, J.G., Connolly, J.L., 2010. Ex vivo imaging of human thyroid pathology using integrated optical coherence tomography and optical coherence microscopy. *J. Biomed. Opt.* 15 (1), 016001–016001.

- Zhou, H., Wang, R., Wang, C., 2008. A novel extended local-binary-pattern operator for texture analysis. *Inf. Sci.* 178 (22), 4314–4325.
- Zysk, A.M., Boppart, S.A., 2006. Computational methods for analysis of human breast tumor tissue in optical coherence tomography images. *J. Biomed Opt.* 11 (5), 054015–054015.
- Zysk, A.M., Chen, K., Gabrielson, E., Tafra, L., May Gonzalez, E.A., Canner, J.K., Schneider, E.B., Cittadine, A.J.P., Carney, S., Boppart, S.A., Tsuchiya, K., Sawyer, K., Jacobs, L.K., 2015. Intraoperative assessment of final margins with a handheld optical imaging probe during breast-conserving surgery may reduce the reoperation rate: results of a multicenter study. *Ann. Surg. Oncol.* 22 (10), 3356–3362.